Signature of room-temperature two-dimensional ferromagnetism in $Ta_{0.67}V_{0.33}Se_2$

Yuhan Du,[1,*] Yuanji Ma,[1,*] Luo-Zhao Zhang,[2] Yiting Liu,[1] Xun Zhu,[1] Qi Feng,[1] Changjian Zhang,[1] Xinyi Wang,[3] Yuxiang Wang,[4] Hongru Wang,[5] Jing Meng,[5] Binglin Liu,[1] Wenbin Wu,[1] Xianghao Meng,[1] Zeping Shi,[1] Lin Sun,[5] Cheng Zhang,[4,6] Xueliang Shi,[3,7] Hai-Bo Yang,[3,7] Hao Shen,[1] Xiaolei Zhang,[1] Qinyuan Jin,[1] Jizhai Cui,[2] Yongfeng Mei,[2] Ying Li,[8] Shengli Zhang,[8] Zhenrong Sun,[1,9] Junhao Chu,[5,9,10] and Xiang Yuan[1,9,11,12,†]

[1]*State Key Laboratory of Precision Spectroscopy, East China Normal University, Shanghai 200241, China*
[2]*Department of Materials Science & State Key Laboratory of Molecular Engineering of Polymers, Fudan University, Shanghai 200438, China*
[3]*Shanghai Key Laboratory of Green Chemistry and Chemical Processes, East China Normal University, Shanghai 200241, China*
[4]*State Key Laboratory of Surface Physics and Institute for Nanoelectronic Devices and Quantum Computing, Fudan University, Shanghai 200433, China*
[5]*Key Laboratory of Polar Materials and Devices, Ministry of Education, East China Normal University, Shanghai 200241, China*
[6]*Zhangjiang Fudan International Innovation Center, Fudan University, Shanghai 201210, China*
[7]*School of Chemistry and Molecular Engineering, East China Normal University, Shanghai 200062, China*
[8]*MOE Key Laboratory for Nonequilibrium Synthesis and Modulation of Condensed Matter, School of Physics, Xi'an Jiaotong University, Xi'an 710049, China*
[9]*School of Physics and Electronic Science, East China Normal University, Shanghai 200241, China*
[10]*Institute of Optoelectronics, Fudan University, Shanghai 200438, China*
[11]*Shanghai Center of Brain-Inspired Intelligent Materials and Devices, Department of Electronics, East China Normal University, Shanghai 200241, China*
[12]*Chongqing Institute of East China Normal University, Chongqing 401120, China*

(Received 6 August 2024; revised 28 September 2024; accepted 1 November 2024; published 25 November 2024)

The discovery of ferromagnetism in van der Waals materials attracts intense research interest and holds profound implications for two-dimensional spintronic devices. However, in most cases the Curie temperature of van der Waals ferromagnets is much lower than room temperature, hindering their potential for device applications. In this study we report the discovery of room-temperature ferromagnetism in layered $Ta_{0.67}V_{0.33}Se_2$. The single crystal is synthesized through the partial replacement of tantalum with vanadium. The crystal structure of $Ta_{0.67}V_{0.33}Se_2$ closely resembles that of both 1T-VSe_2 and 1T-$TaSe_2$. The resultant $Ta_{0.67}V_{0.33}Se_2$ exhibits a Hall sign reversal at around 60 K, with the dominant carrier changing from electron type at higher temperatures to hole type at lower temperatures. The anomalous peak is observed in the longitudinal resistivity near the critical temperature, which is ascribed to the temperature-induced Lifshitz transition. Despite the fact that bulk 1T-VSe_2 and 1T-$TaSe_2$ are paramagnetic, $Ta_{0.67}V_{0.33}Se_2$ displays room-temperature ferromagnetism, as evidenced by the hysteresis behavior observed in the field-dependent magnetization. Collective anomalies are observed at about 60 K in both magnetization and transport measurements, indicating a strong correlation between electric and magnetic degrees of freedom. Moreover, room-temperature ferromagnetism is confirmed in few-layer $Ta_{0.67}V_{0.33}Se_2$ through magneto-optic Kerr measurements. Our work provides a strategy for accessing two-dimensional high-Curie-temperature magnets, which hold promise for potential applications in spintronic devices.

DOI: 10.1103/PhysRevB.110.184427

I. INTRODUCTION

The emergence of van der Waals ferromagnetic materials [1,2] has expanded the family of two-dimensional (2D) materials and pointed out the potential for various spintronic applications, including magnetoresistive random-access memory [3], magnetic sensors [4], and spin valve devices [5].

The screening effect is suppressed in 2D, which facilitates external control of magnetic property by various mechanisms, including strain [6,7], intercalation [8,9], and electromagnetic field [10–12]. In transition-metal dichalcogenides, for instance, magnetic element doping [13–16] and the application of electric fields [13] or lasers [17] have successfully demonstrated the control of magnetic order. In MnX_2 (X = S, Se) [18,19] or CrX_2 (X = Se, Te), stress plays a role in modulating magnetism [20]. Additionally, even a slight change in the number of layers can lead to a drastic variation in the Curie temperature (T_c). In the case of MnSn [21], increasing the number of layers from one to three results in a nearly 200 K increase in T_c.

*These authors contributed equally to this work.
†Contact author: xyuan@lps.ecnu.edu.cn

Thus far, many noteworthy phenomena have been discovered in two-dimensional magnets, laying the foundation for the development of diverse applications in this field. These phenomena include the identification of the quantum anomalous Hall effect in $MnBi_2Te_4$ [22], as well as the recognition of nonreciprocal magneto-phonon effect and two-dimensional magnons in CrI_3 [23] or $CrCl_3$ [24,25]. Experimental breakthroughs have yielded several prototype spintronics devices, opening up promising possibilities for future applications. Notable examples include spin valves based on FeX_2 (X = Cl, Br, I) [26,27] or metasurfaces, CrI_3-based spin filters [28,29], and spin field-effect transistors constructed with CrI_3 or 2H-VX_2 (X = S, Se, Te) [30,31].

The material family with two-dimensional ferromagnetism generally started with low T_c. For instance, widely recognized materials like CrX_3 (X = I, Br) [11,32–34] and $CrXTe_3$ (X = Si, Ge) [10,35–37] exhibit T_c in the tens of Kelvin. Higher T_c are found in $CrSe_2$ nanosheet (110 K) [38,39], GaMnAs (160 K) [40], Fe_3GeTe_2 (200 − 230 K) [41,42]. Only a limited number of materials exhibit ferromagnetic properties with a T_c close to or higher than room temperature. Reported systems encompass $Fe_{5-x}GeTe_2$ ($x = 0$, 1) (260−310 K) [43,44], Fe_3GaTe_2 (367 K) [45], 1T-$CrTe_2$ (300 K) [46], and epitaxially-grown $MnSe_2$ nanofilms (310 K) [47].

Considerable efforts have been devoted to further enhancing T_c. In Fe_3GeTe_2 [48], MnX_2 (X = S, Se) [18], straining leads to changes in bond length and bond angle, thereby affecting the magnetic exchange parameters and raising the T_c. The another strategy entails the introduction of heterostructures, which impacts the proximity coupling effect and interlay charge transfer between interfaces [49–52]. For instance, the $Cr_5Te_8/CrTe_2$ heterostructure has recently demonstrated robust 2D ferromagnetism [53]. Gating technique allows effective modulation, not only on the T_c, but also on the saturation magnetization (M_s) and coercive field (H_c). In the case of bilayer CrI_3, gating not only alters T_c but also transforms the interlayer coupling from antiferromagnetic to ferromagnetic [54,55]. Magnetic doping provides an alternative and yet extrinsic method, where ferromagnetism and high T_c is introduced by adding magnetic atoms (Fe, Co, Ni, Cr, Mn) to the two-dimensional materials [13–16,56–58]. The T_c of most room-temperature 2D ferromagnets is lower than 360 K; a higher T_c might provide better stability and performance of spintronic devices working at room temperature.

In this work we present the synthesis of 2D room-temperature van der Waals magnets $Ta_{0.67}V_{0.33}Se_2$ and the discovery of its room-temperature ferromagnetism in both bulk and few-layer form. The $Ta_{0.67}V_{0.33}Se_2$ single crystal is prepared by chemical vapor transport (CVT), and its stoichiometric composition is characterized using energy-dispersive x-ray spectroscopy (EDS) and x-ray photoelectron spectroscopy (XPS). The crystal structure is found to be identical to that of 1T-$TaSe_2$ and 1T-VSe_2, as confirmed by the x-ray diffraction (XRD), while Raman spectra reveal substantial variations in phonon dynamics. At approximately 60 K, we observe a Hall sign reversal and a peak in longitudinal resistivity, suggesting a possible temperature-induced Lifshitz transition, as such a transition is often associated with resistivity or thermoelectric features [59–64]. Magnetization measurements also illustrate a similar anomaly at 60 K, signaling a strong coupling between electric and magnetic properties. Furthermore, upon sweeping the magnetic field (H) back and forth, we identify prominent and persistent hysteresis up to 400 K, demonstrating the room-temperature ferromagnetism of $Ta_{0.67}V_{0.33}Se_2$ with perpendicular magnetic anisotropy. The room-temperature ferromagnetism persists in the few-layer limit, as evidenced by magneto-optic Kerr measurements. Our work reports a room-temperature 2D ferromagnetic material and paves a step in developing and implementing room-temperature 2D ferromagnetism.

We synthesize $Ta_{0.67}V_{0.33}Se_2$ by partially replacing tantalum with vanadium in 1T-$TaSe_2$. Both $TaSe_2$ and VSe_2 [65,66] are well-known 2D materials that can be easily grown and exfoliated. Of these, 1T-$TaSe_2$ is considered a candidate for quantum spin liquid [67]. In its bulk form, it undergoes a charge-density-wave (CDW) transition at 475 K and forms a $\sqrt{13} \times \sqrt{13}$ superlattice structure [68]. On the other hand, the monolayer $TaSe_2$ exhibits a Mott-insulator-metal transition [69]. Meanwhile, 1T-VSe_2 experiences a similar CDW transition at around 110 K [70]. The transition temperature gradually decreases as the material thickness is reduced [71] but suddenly increases to 135 K in the case of a monolayer [70]. In general, it shows paramagnetic behavior in the bulk form, while the existence of monolayer magnetism is still under debate [72,73].

II. RESULTS AND ANALYSES

As shown in Fig. 1(a), single-crystal $Ta_{0.67}V_{0.33}Se_2$ is prepared by the CVT method. Ta, V, and Se powders were mixed in a molar ratio of 2 : 1 : 6, with iodine serving as the transport agent. The mixture was then sealed in a vacuum quartz tube and placed into a two-zone furnace. After holding for about one week, 5 mm × 5 mm shiny flakes were grown in the cold zone (refer to the Methods section for more details). The chemical ratio of the reactants has minimal impact on the ratio of the product (Ta : V : Se ≈ 2 : 1 : 6), indicating that $Ta_{0.67}V_{0.33}Se_2$ likely possesses a metastable structure. The as-grown crystal is easily exfoliated for subsequent transport and optical experiments.

Similar to the parent compound 1T-VSe_2 and 1T-$TaSe_2$, $Ta_{0.67}V_{0.33}Se_2$ is expected to crystallize in a trigonal crystal structure with the space group $P\bar{3}m1$ [Fig. 1(b)]. To examine the crystal structure and quality of the $Ta_{0.67}V_{0.33}Se_2$ crystal, XRD measurement is conducted, as shown in Fig. 1(c). The green, red, and gray curves represent the XRD patterns of 1T-VSe_2, $Ta_{0.67}V_{0.33}Se_2$, and 1T-$TaSe_2$, respectively. The XRD patterns exhibit similarities across different compounds, and the extracted lattice constant $c = 6.15$ Å of $Ta_{0.67}V_{0.33}Se_2$ lies between the value of 1T-VSe_2 ($c = 6.13$ Å) and 1T-$TaSe_2$ ($c = 6.27$ Å). This similarity is a natural outcome of elementary substitution, which has a minor impact on the lattice constant. The presence of a single set of XRD peaks supports $Ta_{0.67}V_{0.33}Se_2$ as a distinct crystal type rather than a mixture of both $TaSe_2$ and VSe_2 phases. Otherwise, peaks from both compounds would be expected. This is further supported by scanning tunneling microscopy (STM) (Extended Data Fig. 7). The elemental composition of the as-grown samples is determined using EDS spectrum (Extended Data Fig. 8) based

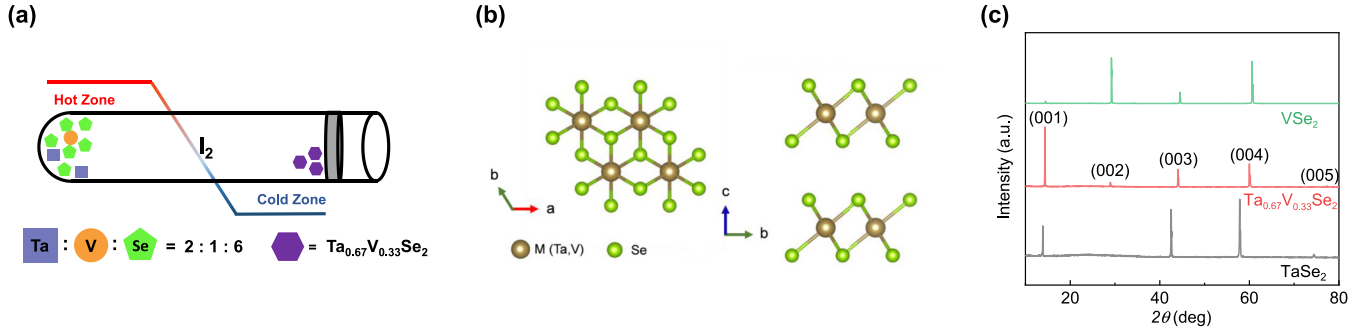

FIG. 1. Crystal structure and characterization of $Ta_{0.67}V_{0.33}Se_2$. (a) Schematic diagram of the chemical vapor transport. (b) Crystal structure of 1T-$TaSe_2$ and 1T-VSe_2. In the as-grown $Ta_{0.67}V_{0.33}Se_2$, Ta atoms are partially substituted by V atoms. (c) X-ray diffraction patterns of VSe_2 (green), $Ta_{0.67}V_{0.33}Se_2$ (red), and $TaSe_2$ (gray). It suggests that the lattice structure remains nearly identical during the elementary substitution. The coexistence of 1T-$TaSe_2$ and 1T-VSe_2 phases can be ruled out. Otherwise, the peaks of both 1T-$TaSe_2$ and 1T-VSe_2 would appear.

on the scanning electron microscope (SEM). The crystal is found to exclusively consist of Ta, V, and Se. Based on the EDS spectra and elemental mapping images [Extended Data Figs. 8(b) and 8(c)], the stoichiometric ratio is determined to be Ta : V : Se = 22.5 : 13.3 : 64.2, and the results are repeatable within the same batch. The composition of Se element is slightly lower than expected, suggesting the existence of Se vacancies.

The XRD spectrum provides information on the crystal structure and lattice constant, while Raman spectroscopy is more sensitive to elementary substitution. For space group $P\bar{3}m1$, the irreducible representation of the corresponding vibrational modes is written as [74–77], $\Gamma = A_{1g} + E_g(2) + 2A_{2u} + 2E_u(2)$, where A_{1g} and E_g are Raman active, A_{2u} and E_u are infrared active. Here, both of $E_g(2)$ and $E_u(2)$ denote doubly degenerate modes. Figure 2(a) shows comparative Raman spectra of $Ta_{1-x}V_xSe_2$ ($x = 0, 0.33, 1$). The A_{1g} (207 cm^{-1}) mode is observed in VSe_2, while the E_g mode is negligibly weak at room temperature [78]. The inset in Fig. 2(a) exhibits the out-of-plane vibrational mode of Se atoms (A_{1g}). Similarly, the spectrum feature near 187 cm^{-1} of $TaSe_2$ corresponds to the A_{1g} mode. The Raman spectrum of $Ta_{0.67}V_{0.33}Se_2$ shows distinct features of peaks at 180 cm^{-1} and 230 cm^{-1}, which agrees with the sensitivity of the Raman spectrum upon chemical substitution.

XPS is conducted to further investigate the elementary composition. The dotted, green, and purple curves present the raw data, background, and fitting results, respectively. Ta-4f core levels are displayed in Fig. 2(b). The peaks (in red) corresponding to Ta-4$f_{7/2}$ and Ta-4$f_{5/2}$ are located at 23.8 eV and 25.7 eV, respectively, indicating a +4 valence state for Ta [79,80] and a 1.9-eV spin-orbital splitting. Two blue peaks, 4$f_{7/2}$ and 4$f_{5/2}$, at the binding energies of 26.5 eV and 28.4 eV, are caused by the inevitable oxidation under ambient atmosphere [80]. Furthermore, the prominent features in Fig. 2(c) are the twin peaks (pink and blue) corresponding to V-2$p_{3/2}$ (517 eV) and V-2$p_{1/2}$ (524 eV), indicating the presence of solely +4 valence state for V [81]. The doublet in Fig. 2(d) matches Se-3$d_{5/2}$ (55.0 eV) and Se-3$d_{3/2}$ (55.9 eV), confirming the presence of Se^{2-}. These findings collectively demonstrate that the crystals contain Ta^{4+}, V^{4+}, and Se^{2-} bonds, except for the oxidized part.

Transport measurements are carried out to probe the electrical properties of $Ta_{0.67}V_{0.33}Se_2$. Thin flakes with a thickness on the order of 100 nm are obtained through mechanical exfoliation. A standard Hall bar device is fabricated by photolithography. The experimental configuration is illustrated in the schematic plot [inset in Fig. 3(a)], where the AC current is applied along the a axis and the magnetic field is maintained parallel to the c axis. Figure 3(a) presents the normalized temperature-dependent longitudinal resistivity, revealing an apparent peak around 60 K. Meanwhile, Hall resistivity (ρ_{xy}) [Fig. 3(b)] exhibits a sign reversal around this temperature, with the slope changing from positive at low temperatures to negative at high temperatures. The Hall coefficient ($R_H = \rho_{xy}/B$) in Fig. 3(c) is obtained by the linear fitting of ρ_{xy}. The blue and orange colors indicate the hole-dominating regime at lower temperatures and the electron-dominating regime at high temperatures, respectively.

Upon closer examination of the Hall resistivity, a nonlinear response to the magnetic field becomes apparent. As depicted in Fig. 3(d), the Hall resistivity at 30 K (upper first panel) exhibits a perfectly linear response with a positive slope, indicating single-hole-carrier transport. At 60 K and 85 K (upper second and third panel), Hall resistivity deviates from linearity with sign reversal around transition temperature. It implies that carriers do not simply transition from a single-electron to single-hole state near the transition temperature but undergo a coexistence and competition. At a much higher temperature (upper fourth panel), the Hall resistivity once again returns to a perfect linear relationship, but with a negative slope. To quantitatively analyze the two-carrier transport, a two-band model [82,83] was employed to fit the Hall resistivity:

$$\rho_{xy} = \frac{1}{e}\frac{\left[\mu_h^2 n_h - \mu_e^2 n_e\right]\mu_0 H + \mu_h^2\mu_e^2(n_h - n_e)\mu_0^3 H^3}{\left[\mu_h n_h + \mu_e n_e\right]^2 + \mu_h^2\mu_e^2(n_h - n_e)^2\mu_0^2 H^2},$$

where e represents the electron charge, and n_e (n_h) denotes the electron (hole) carrier concentration. Similarly, μ_e (μ_h) stands for the electron (hole) mobility. The fitting results are presented in Fig. 3(e). At low temperatures, only hole carriers are involved. Thereafter, as the temperature rises, a gradual increase in the electron concentration (red curve) is

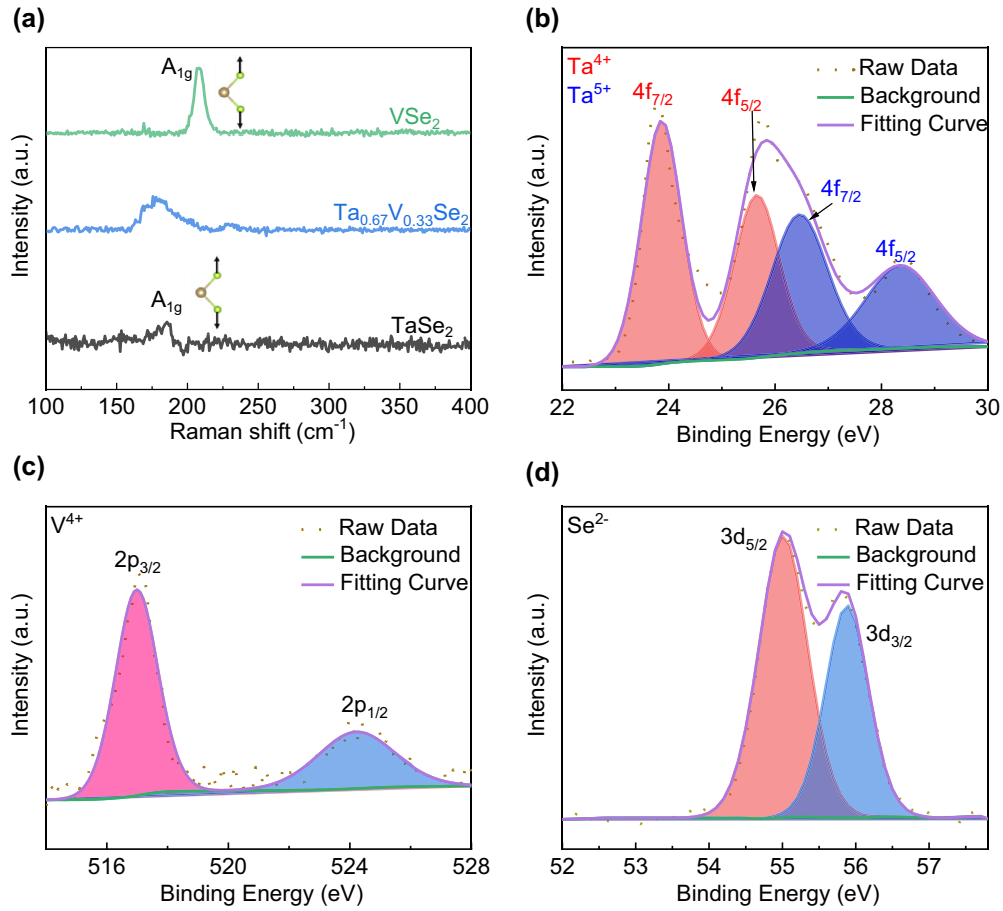

FIG. 2. Raman and XPS spectra of $Ta_{0.67}V_{0.33}Se_2$. (a) The Raman spectra of VSe_2, $Ta_{0.67}V_{0.33}Se_2$, $TaSe_2$ thin flakes. The identified vibrational modes are labeled near the peaks. (b)–(d) The XPS spectra of $Ta_{0.67}V_{0.33}Se_2$. (b) Ta-4f core levels. The red and blue peaks mark the binding energy of Ta^{4+} and Ta^{5+}, respectively. (c) 2p peaks of V^{4+}. Pink peak marks V-2$p_{3/2}$, and blue peak marks V-2$p_{1/2}$. (d) 3d peaks of Se^{2-}. Se-3$d_{5/2}$ and Se-3$d_{3/2}$ are shown as red and blue peaks, respectively.

accompanied by a decrease in the hole concentration (blue curve). The two curves intersect at around 60 K and then reach saturation above 120 K. At the high-temperature end, electrons solely contribute to the conductivity.

The overall temperature dependence of longitudinal resistivity and Hall resistivity can be explained by a temperature-induced Lifshitz transition. This transition occurs in a metallic system that has both electron and hole pockets with finite overlap on the energy scale. At a low temperature [lower first panel in Fig. 3(d)], the Fermi level only crosses the hole pockets, leading to single carrier transport. As the temperature increases, the Fermi level rises, leading to a Lifshitz transition between 30 K and 60 K. This transition causes the number of Fermi surfaces to change from one to two, but it does not cause an abrupt change in the resistivity unless the quantum oscillation is observed. At 60 K (lower second panel), the Fermi level starts to intersect with the conduction band, while the valance band still dominates the transport. Therefore, holes act as the major carriers, while the presence of electrons leads to the deviation from the linear Hall response. At the transition temperature, where the contributions of the conduction and valence bands are compensated, a Hall sign reversal occurs. The compensation of the carriers also induces the longitudinal resistivity to reach its maximum. At higher temperatures, the Fermi energy continually rises away from the valence band (lower third and fourth panels), resulting in single-electron transport behavior.

Due to the presence of the magnetic element, vanadium, we explore the magnetic properties of $Ta_{0.67}V_{0.33}Se_2$ by superconducting quantum interference device (SQUID). The magnetization in both the out-of-plane and in-plane configurations is measured as a function of temperature, revealing distinct behavior [Fig. 4(a)]. In the out-of-plane configuration, the zero-field cooling (ZFC) curve (in red) does not overlap with the field cooling (FC) curve (in gray) throughout the entire experimental regime (2–400 K), indicating thermomagnetic irreversibility. In contrast, the two curves almost overlap in the in-plane configuration. Thus, $Ta_{0.67}V_{0.33}Se_2$ possesses long-range magnetism with perpendicular magnetic anisotropy. Furthermore, collective anomalies are found in both transport and magnetization, as shown in Fig. 4(b). The Hall coefficient undergoes a sign change, and the longitudinal resistivity has a peak (upper panel), while the magnetization shows a similar anomalous peak at around 60 K (bottom panel). This implies a correlation between the electric and magnetic degree of freedom in $Ta_{0.67}V_{0.33}Se_2$, possibly originating from itinerant magnetism with the Stoner mechanism [84]. When the Fermi level crosses both the edge of the

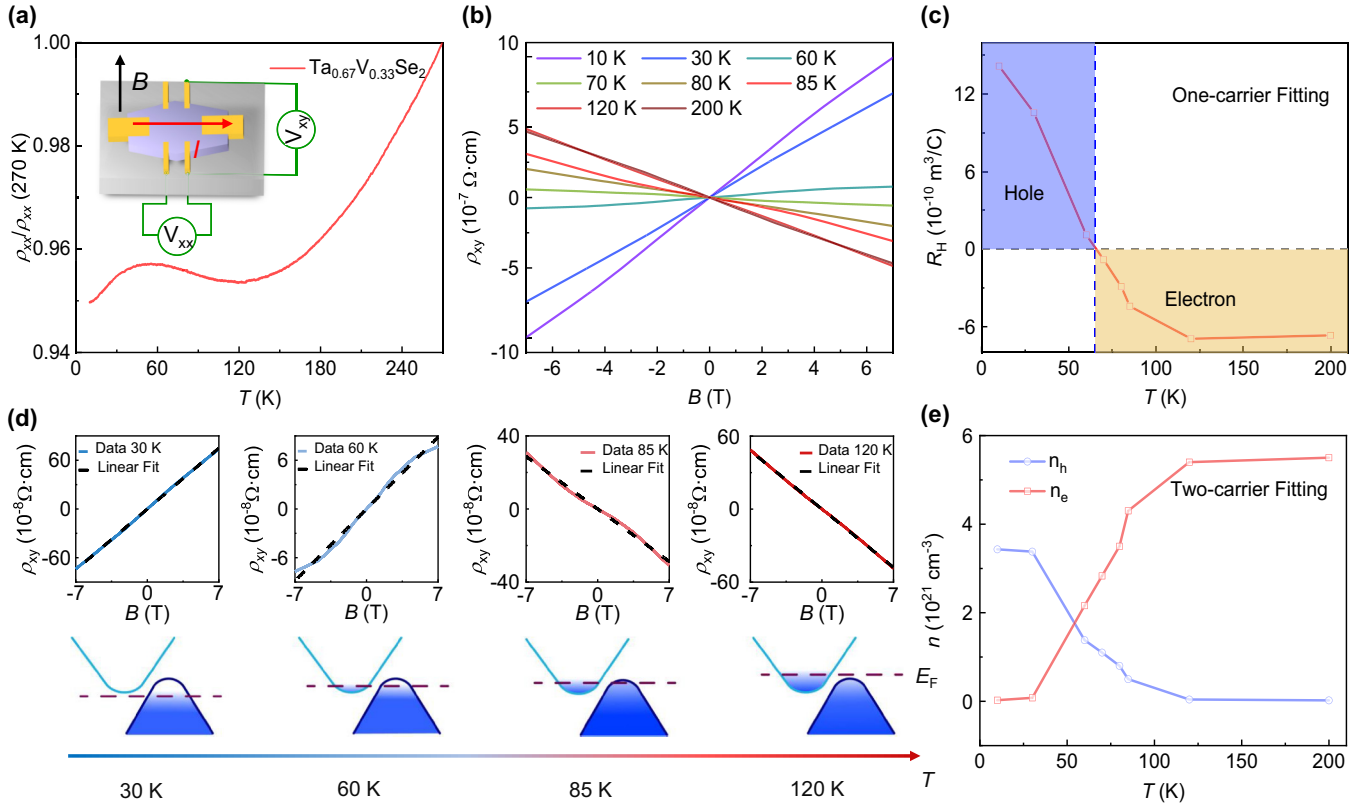

FIG. 3. Magnetotransport measurement of $Ta_{0.67}V_{0.33}Se_2$ films. (a) Temperature dependence of normalized longitudinal resistivity. A resistivity peak is observed around 60 K. The inset is the sketch of the standard Hall bar device and experimental configuration. (b) Hall resistivity ρ_{xy} at different temperatures, showing sign reversal around 60 K. (c) Temperature dependence of Hall coefficient R_H extracted by linear fitting of ρ_{xy}. Dominating carrier type changes from electron at higher temperatures to hole at lower temperatures. (d) Hall resistivity at typical temperature and corresponding energy band diagram. The blue and red solid lines in upper panels are Hall data from experiments, and the black dashed lines are the linear fitting. At the lowest and highest temperature, the Hall resistivity is perfectly linear with the magnetic field, despite the opposite sign of the slope. Close to the temperature regime of Hall sign reversal and longitudinal resistivity peak, the Hall resistivity deviates away from linearity, indicating the two-carrier transport. The observed Hall and longitudinal behavior can be explained by the temperature-induced Lifshitz transition, as shown in the bottom panel. The slight overlap between the conduction band and valence band allows both types of carriers to be near the transition temperature and explains the single-carrier transport at much higher and lower temperatures. (e) Temperature-dependent carrier concentration fitted from the two-band model. The red and blue curves denote electron concentration and hole concentration, respectively. Near the critical temperature, both types of carriers contribute to the transport.

conduction and valence bands at the critical temperature, the density of states is maximized, leading to a strong modulation of the magnetization.

Temperature-dependent M-H measurements present long-lasting hysteresis, as shown in Fig. 5(a), over a temperature range of 2 K to 400 K. To enhance visualization of the hysteresis at high temperatures, the curves above 300 K are magnified by a factor of 5. The persistence of hysteresis over 350 K and the thermomagnetic irreversibility in the M-T curve indicate the room-temperature ferromagnetic properties of $Ta_{0.67}V_{0.33}Se_2$. Notably, the M-H curve exhibits a typical magnetic biphasic response below 300 K. To separate these components, we fit the experimental M-H curves [Fig. 5(b)] by a two-component Curie-Weiss model [85] $M = M_1 + M_2 = A_1 \cdot \tanh[B_1 \cdot (H \pm C_1)] + A_2 \cdot \tanh[B_2 \cdot (H \pm C_2)]$, where A represents the intensity of saturation magnetization (M_F), C denotes the coercive field (H_F), and the subscript denotes the component index. The fitting curve in Fig. 5(b) agrees with the experimental curve [Fig. 5(a)], supporting the biphasic characteristics of the $Ta_{0.67}V_{0.33}Se_2$. The decoupled components at typical temperature (2 K) are plotted in Extended Data Fig. 9. The fitted M_F and H_F from both components decrease as the temperature increases. The saturation magnetic moment of phase 1 is almost double the value of phase 2. This value ($A_1/A_2 \approx 2$) remains stable as temperature varies. On the contrary, the coercive field of phase 1 is much larger than phase 2. The difference is maximized at low temperatures. Thus, phase 1 dominates the overall magnetic behavior of the system, while phase 2 mainly determines the low-field response due to a small coercive field around 200 Oe. In retrospect, the transport results (Fig. 3) of the thin flake of $Ta_{0.67}V_{0.33}Se_2$ did not directly provide evidence of magnetism, which could be attributed to the overall weak magnetization strength of the system.

Since the room-temperature ferromagnetic and exfoliative properties have been verified in bulk $Ta_{0.67}V_{0.33}Se_2$, it is reasonable and intriguing to anticipate high-T_c ferromagnetism in few layers. We perform the magneto-optical Kerr experiment

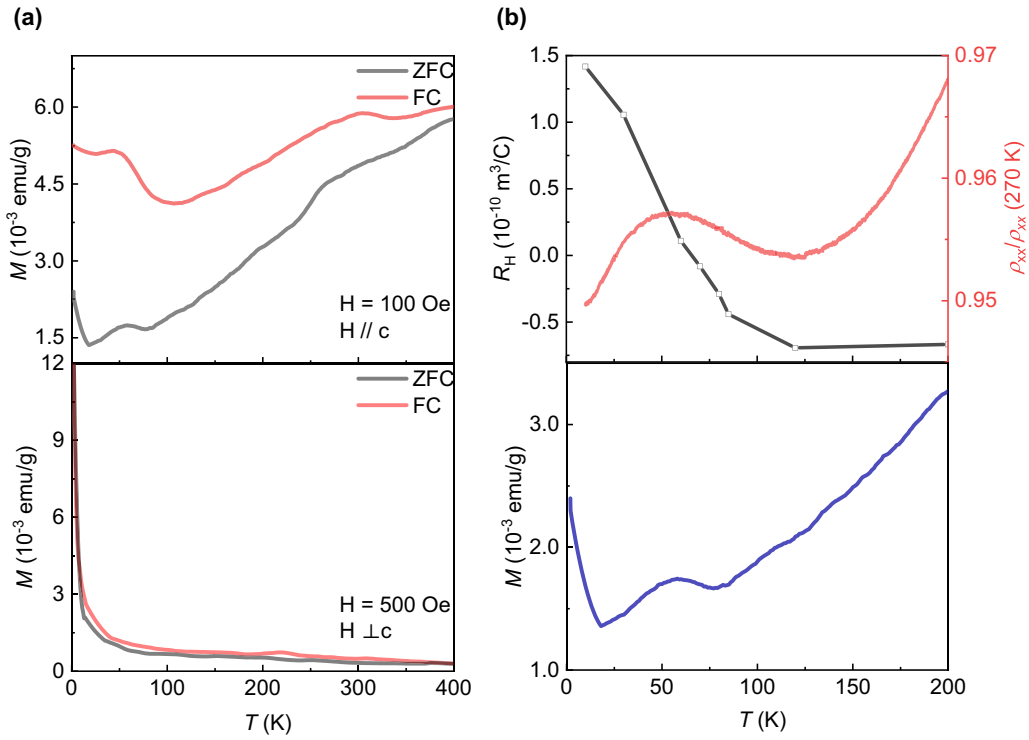

FIG. 4. Ferromagnetism of the $Ta_{0.67}V_{0.33}Se_2$. (a) Temperature-dependent magnetization measurement (ZFC and FC) under out-of-plane field (upper panel) and in-plane field (bottom panel). (b) Temperature-dependent Hall coefficient, longitudinal resistivity, and magnetization. A collective anomaly is found at around 60 K, including (1) an anomalous peak in magnetization, (2) Hall sign reversal, and (3) an anomalous peak in longitudinal resistivity, which indicates the strong coupling between electric and magnetic degrees of freedom.

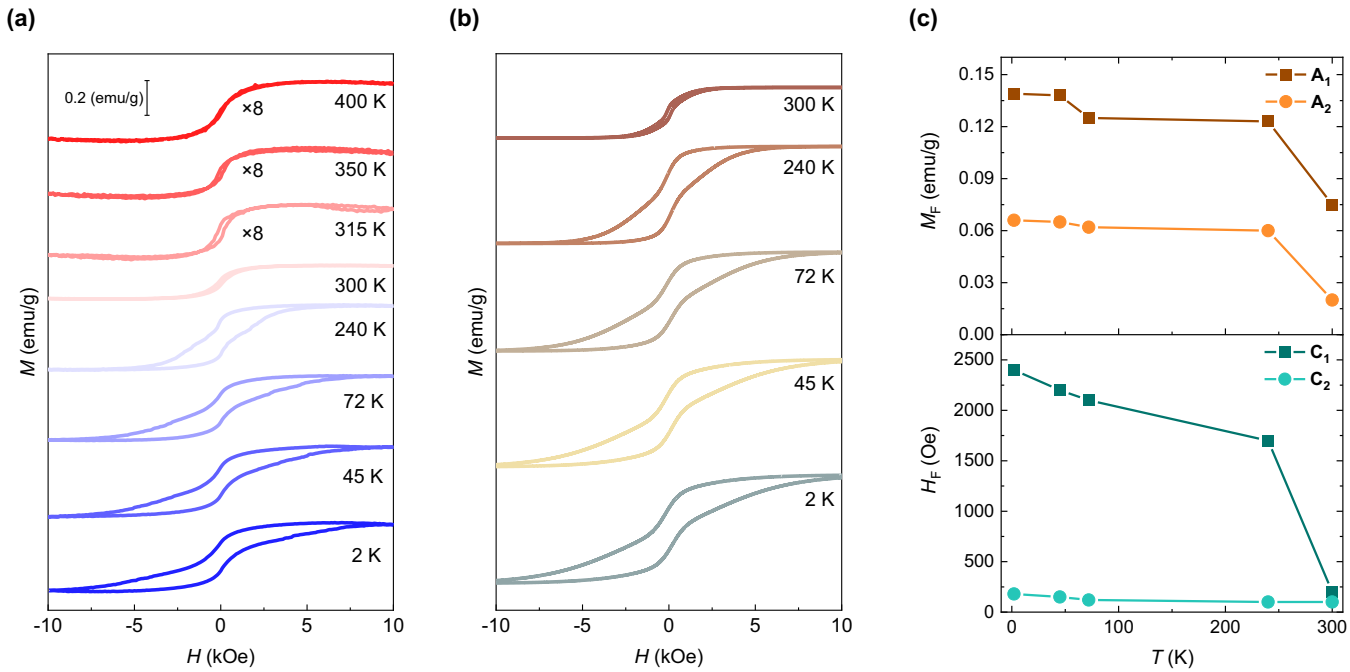

FIG. 5. Temperature-dependent *M*-*H* curves of the $Ta_{0.67}V_{0.33}Se_2$. (a) Out-of-plane *M*-*H* curves at different temperatures. The long-lasting hysteresis points out room-temperature ferromagnetism. (b) *M*-*H* curve-fitting graph in the range of 2 K to 300 K. (c) Temperature-dependent variation of fitting parameters. As the temperature increases, the saturation magnetization and coercive field both decrease monotonically.

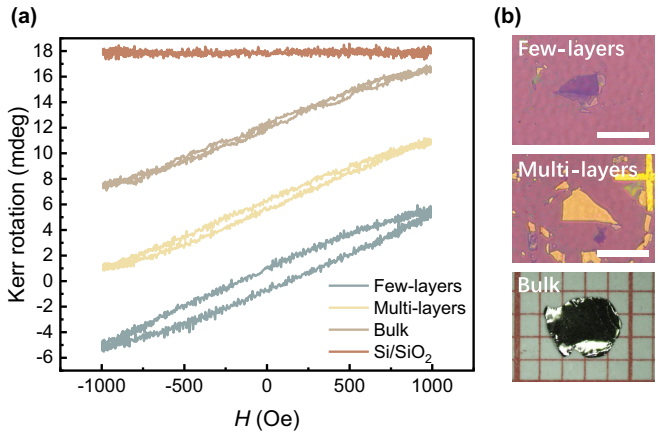

FIG. 6. Magneto-optic Kerr effect (MOKE) measurement of the $Ta_{0.67}V_{0.33}Se_2$. (a) MOKE hysteresis loops measured from few layers to bulk. The measurement is conducted at the room temperature ($T = 300$ K). (b) Images of few layers, multilayers, and bulk $Ta_{0.67}V_{0.33}Se_2$. The length of the white scale is 30 μm, and each grid on the graph paper represents 1 mm. All images correspond to the curves in (a).

on $Ta_{0.67}V_{0.33}Se_2$ of different thicknesses at room temperature (Fig. 6). The samples are prepared by mechanical exfoliation, and thickness is determined by optical contrast. It is evident that all samples exhibit a prominent Kerr rotation compared to the background signal of the Si/SiO_2 substrate. It excludes the possibility that the Kerr rotation and hysteresis originated from either the substrate or the measurement system. This corroborates the presence of room-temperature

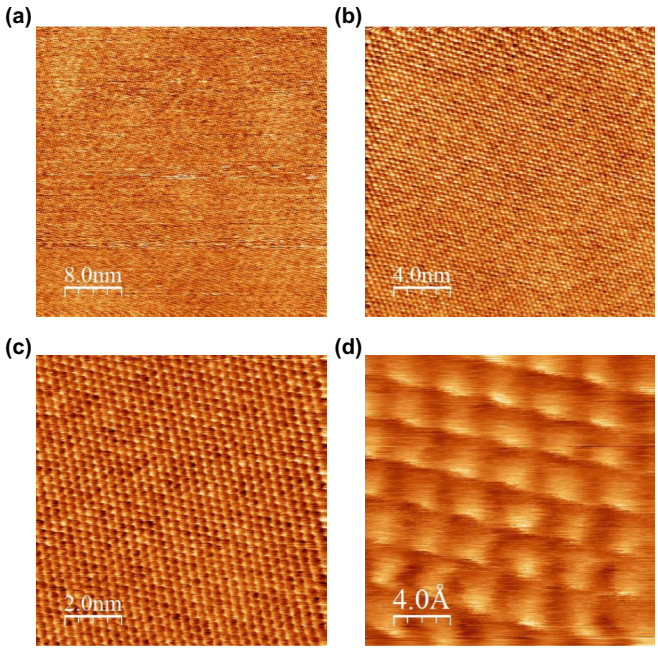

FIG. 7. Scanning tunneling microscopy (STM) of the $Ta_{0.67}V_{0.33}Se_2$. Images were taken in four different scales: (a) 40 nm, (b) 20 nm, (c) 10 nm, and (d) 2 nm. The sample was measured at $V = -1.5$ V and $I = 10$ pA at liquid nitrogen temperature.

ferromagnetic properties in $Ta_{0.67}V_{0.33}Se_2$, regardless of few-layer or bulk forms. Furthermore, it is noteworthy that the coercive field gradually increases as the number of layers decreases. This phenomenon agrees with previous findings in other 2D magnetic systems [84,86–91] and can be attributed to the influence of the structure of magnetic domains in a few studies [92,93].

Moreover, the presence of long-range magnetic order in $Ta_{0.67}V_{0.33}Se_2$ is surprising, since none of the bulk $TaSe_2$ and VSe_2 is ferromagnetic at room temperature. To clarify the potential magnetic sources in the system, we carried out first-principles calculations. The lattice structure used in the computation is based on a supercell comprising three unit cells of VSe_2 [94], where two of the three V atoms are replaced by Ta atoms to form $Ta_{0.67}V_{0.33}Se_2$ (see Extended Data Fig. 10). The calculated energy of the ferromagnetic state E_{FM} is lower than that of the nonmagnetic state E_{NM} ($E_{FM} - E_{NM} \approx -0.4$ eV per formula unit). The magnetic moment per V atom is 1.84 μ_B, which could be affected by both Se vacancies and dimensionality reduction from bulk to monolayer structure. In the case of including Se6 vacancies, the magnetic moment almost does not change but could be increased to 2.39 μ_B if switching V and Ta positions. In the case of using a monolayer sample, the magnetic moment becomes larger (1.91 μ_B), which is caused by a larger Coulomb repulsion arising from the lack of interlayer interactions as suggested from the case of VSe_2 [95]. The theoretical finding demonstrates that the ferromagnetism in $Ta_{0.67}V_{0.33}Se_2$ arises from the interplay between the localized magnetic moments of V and the magnetic moments induced by Se vacancies, which agree with previous studies [96–101] on $PtSe_2$, VSe_2, and $NbSe_2$, where the occurrence of magnetic moments are associated with Se vacancies. It is essential to acknowledge that the first-principles calculations at this stage provide a possible intuitive understanding. The preliminary calculations mentioned above do not exclude the possibility of more complex defect configurations or magnetic structures in the $Ta_{0.67}V_{0.33}Se_2$.

Given its intriguing and persistent room-temperature magnetism, we find it pertinent to explore the potential for manipulating the magnetic properties in $Ta_{0.67}V_{0.33}Se_2$ through future research endeavors. The notable collective anomalies underscore the robust electromagnetic coupling within the system, thereby suggesting the feasibility of electrical control via static-electrical gating. Additionally, altering the Ta-to-V ratio holds promise as an effective strategy for enhancing our comprehension of the magnetism in the $Ta_{1-x}V_xSe_2$ system.

In summary, we report the synthesis and characterization of $Ta_{0.67}V_{0.33}Se_2$, a van der Waals material with room-temperature ferromagnetism. Single crystals are prepared by the CVT method, and the elemental composition is confirmed by XPS and EDS techniques. Structural analysis through XRD and Raman spectroscopy reveals that $Ta_{0.67}V_{0.33}Se_2$ adopts the 1-T phase, consistent with the parent materials 1T-$TaSe_2$ and 1T-VSe_2. We observe a longitudinal resistivity peak and anomalous Hall sign reversal around 60 K, phenomena that can be explained by a temperature-induced Lifshitz transition. Magnetization measurements confirm room-temperature ferromagnetism through thermomagnetic irreversibility in the M-T measurement and a

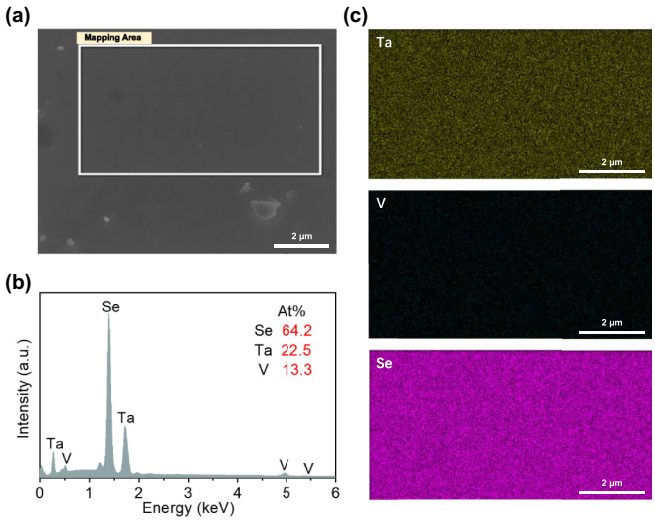

FIG. 8. Energy-dispersive x-ray spectroscopy (EDS) of the as-grown $Ta_{0.67}V_{0.33}Se_2$. (a) Scanning electron microscopy (SEM) image of $Ta_{0.67}V_{0.33}Se_2$. (b) EDS spectrum of $Ta_{0.67}V_{0.33}Se_2$. The stoichiometric ratio is extracted accordingly and found to be consistent within the batch of samples. The proportion of Se is slightly lower than the theoretically expected stoichiometric ratio, suggesting the possible presence of Se vacancies. (c) Elemental mapping of Ta, V, and Se.

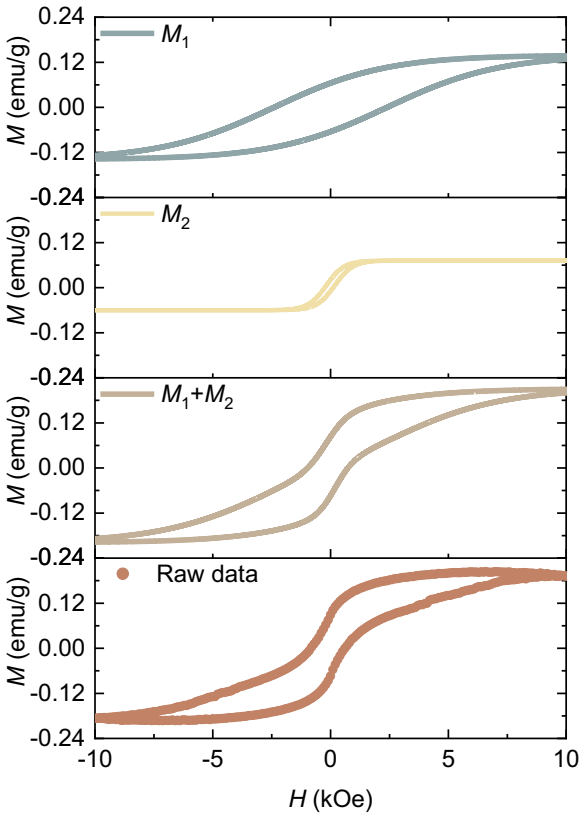

FIG. 9. Decoupled components of M-H curves at 2 K. M_1 and M_2 represent the contribution of each phase alone in $Ta_{0.67}V_{0.33}Se_2$. The experimentally obtained hysteresis curves originate from the sum of M_1 and M_2.

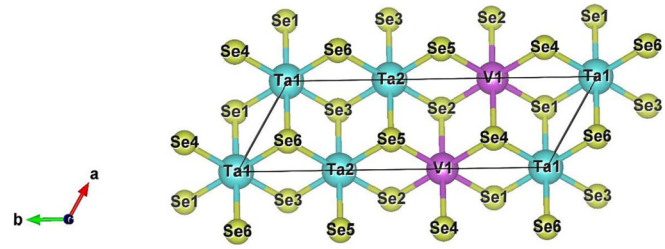

FIG. 10. The hypothetical crystal structures of $Ta_{0.67}V_{0.33}Se_2$ used in first-principle calculations.

persistent hysteresis in the M-H measurement. Interestingly, we note a similar anomaly in the magnetization at the temperature of Hall sign reversal and resistivity peak, indicating the strong electromagnetic coupling within $Ta_{0.67}V_{0.33}Se_2$. Magneto-optic Kerr measurements demonstrate that the room-temperature ferromagnetism extends from bulk to few layers with thickness-dependent coercive field variation. Our study identifies $Ta_{0.67}V_{0.33}Se_2$ as a promising candidate for a room-temperature 2D ferromagnet and paves the way toward room-temperature van der Waals spintronic devices.

III. METHODS

A. Crystal growth and magnetization measurements

Bulk single-crystal $Ta_{0.67}V_{0.33}Se_2$ was obtained by the CVT method. Ta, V, and Se powders are prepared in a stoichiometric ratio. Iodine was used as the transport agent. The mixture was sealed in a vacuum quartz tube and subsequently placed into a two-zone furnace. The hot zone was heated to 950 °C at the speed of 5 °C/min and maintained at 950 °C for 7 days. Similarly, the temperature of the cold zone was raised to 750 °C at the same speed and kept for a week. Finally, the furnace was cooled to room temperature, and single crystals were obtained at the cold zone.

B. Crystal characterization

Raman spectra were measured for the exfoliated thin films on a home-built system with a 632.8-nm He-Ne laser source. The single-crystal structure was characterized by x-ray diffraction (Bruker D8 Discover). $Ta_{0.67}V_{0.33}Se_2$ lattice constants were obtained based on the Visualization for Electronic and STructural Analysis (VESTA) software [102]. Elemental compositions were analyzed by energy-dispersive x-ray spectroscopy with scanning electron microscopy (GeminiSEM 450). XPS was performed using PHI 5000 Versa Probe III. Magnetization was measured by the SQUID (MPMS, Quantum Design) with tunable temperature from 2 K to 400 K. Magneto-optic Kerr effect measurement was performed on NanoMOKE3. Scanning tunneling microscopy is used to characterize the surface information of $Ta_{0.67}V_{0.33}Se_2$ crystal. The sample was measured at $V = -1.5$ V and $I = 10$ pA at liquid nitrogen temperature.

C. Sample fabrication and transport measurements

$Ta_{0.67}V_{0.33}Se_2$ nanosheets were mechanically exfoliated onto Si/SiO_2 substrate. The Hall bar device is fabricated

using home-built photolithography. Cr (3 nm) and Au (70 nm) are deposited as electrodes. Magnetotransport measurements were performed at Oxford TeslatronPT cryostat with Stanford Research SR-860 lock-in amplifier.

D. First-principles calculations

The total energy and electronic structure are calculated with the projector-augmented-wave basis as implemented in the Vienna Ab initio Simulation Package (VASP) [103,104]. The structure was constructed as a supercell including three unit cells [94] of VSe_2 along replacing two of the three V by Ta (see Extended Data Fig. 10). Each supercell has two V, one Ta, and six Se, labeled as Ta1-Ta2, V1, Se1-Se6, respectively. The Se vacancy in the Se6 positions and two-dimensional monolayer were also considered. The generalized gradient approximation [105] for the exchange-correlation function and energy cutoff of 400 eV were used. Hubbard correction effects were included on a mean-field level in the rotationally invariant implementation of the GGA+U method [106] with U = 3 eV for V and 2 eV for Ta. A Γ-centered $20 \times 6 \times 10$ mesh in the Brillouin zone was sampled for the bulk structures and $20 \times 6 \times 4$ for the monolayer structure.

The data that support the findings of this study are available upon reasonable request from the authors.

ACKNOWLEDGMENTS

This research was sponsored by the National Key R&D Program of China (Grant No. 2023YFA1407500), Shanghai Pilot Program for Basic Research (Grant No. TQ20240203), the National Natural Science Foundation of China (Grant No. 12174104), Shanghai Rising-Star Program Grant No. 24QA2702200, Natural Science Foundation of Chongqing (Grant No. cstc2021jcyj-msxmX0668), Shuguang Project, the Fundamental Research Funds for the Central Universities (Grant No. xzy012023051), and HPC Platform, Xi'an Jiaotong University.

The authors declare no competing financial interest.

[1] K. S. Burch, D. Mandrus, and J.-G. Park, Magnetism in two-dimensional van der Waals materials, Nature (London) **563**, 47 (2018).

[2] M. Gibertini, M. Koperski, A. F. Morpurgo, and K. S. Novoselov, Magnetic 2D materials and heterostructures, Nat. Nanotechnol. **14**, 408 (2019).

[3] D. Apalkov, B. Dieny, and J. M. Slaughter, Magnetoresistive random access memory, Proc. IEEE **104**, 1796 (2016).

[4] J. Lenz and S. Edelstein, Magnetic sensors and their applications, IEEE Sensors J. **6**, 631 (2006).

[5] X. Lin, W. Yang, K. L. Wang, and W. Zhao, Two-dimensional spintronics for low-power electronics, Nat. Electron. **2**, 274 (2019).

[6] Z. Li, B. Zhou, and C. Luan, Strain-tunable magnetic anisotropy in two-dimensional Dirac half-metals: Nickel trihalides, RSC Adv. **9**, 35614 (2019).

[7] Z. Wu, J. Yu, and S. Yuan, Strain-tunable magnetic and electronic properties of monolayer CrI_3, Phys. Chem. Chem. Phys. **21**, 7750 (2019).

[8] D. Weber, A. H. Trout, D. W. McComb, and J. E. Goldberger, Decomposition-induced room-temperature magnetism of the Na-intercalated layered ferromagnet $Fe_{3-x}GeTe_2$, Nano Lett. **19**, 5031 (2019).

[9] M. Yang, Q. Li, R. V. Chopdekar, C. Stan, S. Cabrini, J. W. Choi, S. Wang, T. Wang, N. Gao, A. Scholl, N. Tamura, C. Hwang, F. Wang, and Z. Qiu, Highly enhanced Curie temperature in Ga-implanted Fe_3GeTe_2 van der Waals material, Adv. Quantum Technol. **3**, 2000017 (2020).

[10] I. A. Verzhbitskiy, H. Kurebayashi, H. Cheng, J. Zhou, S. Khan, Y. P. Feng, and G. Eda, Controlling the magnetic anisotropy in $Cr_2Ge_2Te_6$ by electrostatic gating, Nat. Electron. **3**, 460 (2020).

[11] P. Jiang, L. Li, Z. Liao, Y. X. Zhao, and Z. Zhong, Spin direction-controlled electronic band structure in two-dimensional ferromagnetic CrI_3, Nano Lett. **18**, 3844 (2018).

[12] J. Shen, J. Gao, C. Yi, M. Li, S. Zhang, J. Yang, B. Wang, M. Zhou, R. Huang, H. Wei, H. Yang, Y. Shi, X. Xu, H.-J. Gao, B. Shen, G. Li, Z. Wang, and E. Liu, Magnetic-field modulation of topological electronic state and emergent magnetotransport in a magnetic Weyl semimetal, The Innovation **4**, 100399 (2023).

[13] S. J. Yun, D. L. Duong, D. M. Ha, K. Singh, T. L. Phan, W. Choi, Y.-M. Kim, and Y. H. Lee, Ferromagnetic order at room temperature in monolayer WSe_2 semiconductor via vanadium dopant, Adv. Sci. **7**, 1903076 (2020).

[14] F. Zhang, B. Zheng, A. Sebastian, D. H. Olson, M. Liu, K. Fujisawa, Y. T. H. Pham, V. O. Jimenez, V. Kalappattil, L. Miao, T. Zhang, R. Pendurthi, Y. Lei, A. L. Elías, Y. Wang, N. Alem, P. E. Hopkins, S. Das, V. H. Crespi, M. Phan, and M. Terrones, Monolayer vanadium-doped tungsten disulfide: A room-temperature dilute magnetic semiconductor, Adv. Sci. **7**, 2001174 (2020).

[15] Y. T. H. Pham, M. Liu, V. O. Jimenez, Z. Yu, V. Kalappattil, F. Zhang, K. Wang, T. Williams, M. Terrones, and M.-H. Phan, Tunable ferromagnetism and thermally induced spin flip in vanadium-doped tungsten diselenide monolayers at room temperature, Adv. Mater. **32**, 2003607 (2020).

[16] S. Fu, K. Kang, K. Shayan, A. Yoshimura, S. Dadras, X. Wang, L. Zhang, S. Chen, N. Liu, A. Jindal, X. Li, A. N. Pasupathy, A. N. Vamivakas, V. Meunier, S. Strauf, and E.-H. Yang, Enabling room temperature ferromagnetism in monolayer MoS_2 via in situ iron-doping, Nat. Commun. **11**, 2034 (2020).

[17] V. Ortiz Jimenez, Y. T. H. Pham, M. Liu, F. Zhang, Z. Yu, V. Kalappattil, B. Muchharla, T. Eggers, D. L. Duong, M. Terrones, and M.-H. Phan, Light-controlled room temperature ferromagnetism in vanadium-doped tungsten disulfide semiconducting monolayers, Adv. Electron. Mater. **7**, 2100030 (2021).

[18] M. Kan, S. Adhikari, and Q. Sun, Ferromagnetism in MnX_2 (X = S, Se) monolayers, Phys. Chem. Chem. Phys. **16**, 4990 (2014).

[19] Q. Li, C. Zhang, D. Wang, K.-Q. Chen, and L.-M. Tang, Giant valley splitting in a $MoTe_2/MnSe_2$ van der Waals

heterostructure with room-temperature ferromagnetism, Mater. Adv. **3**, 2927 (2022).

[20] H. Y. Lv, W. J. Lu, D. F. Shao, Y. Liu, and Y. P. Sun, Strain-controlled switch between ferromagnetism and antiferromagnetism in 1T-Cr_2 (Se, Te) monolayers, Phys. Rev. B **92**, 214419 (2015).

[21] P. Feng, X. Zhang, S. Zhang, D. Liu, M. Gao, F. Ma, X.-W. Yan, and Z.-Y. Xie, Interlayer coupling induced sharp increase of the Curie temperature in a two-dimensional MnSn multilayer, ACS Omega **7**, 43316 (2022).

[22] Y. Deng, Y. Yu, M. Z. Shi, Z. Guo, Z. Xu, J. Wang, X. H. Chen, and Y. Zhang, Quantum anomalous Hall effect in intrinsic magnetic topological insulator $MnBi_2Te_4$, Science **367**, 895 (2020).

[23] Z. Liu, K. Guo, G. Hu, Z. Shi, Y. Li, L. Zhang, H. Chen, L. Zhang, P. Zhou, H. Lu, M.-L. Lin, S. Liu, Y. Cheng, X. L. Liu, J. Xie, L. Bi, P.-H. Tan, L. Deng, C.-W. Qiu, and B. Peng, Observation of nonreciprocal magnetophonon effect in nonencapsulated few-layered CrI_3, Sci. Adv. **6**, eabc7628 (2020).

[24] J. Cenker, B. Huang, N. Suri, P. Thijssen, A. Miller, T. Song, T. Taniguchi, K. Watanabe, M. A. McGuire, D. Xiao, and X. Xu, Direct observation of two-dimensional magnons in atomically thin CrI_3, Nat. Phys. **17**, 20 (2021).

[25] M. Augustin, S. Jenkins, R. F. L. Evans, K. S. Novoselov, and E. J. G. Santos, Properties and dynamics of meron topological spin textures in the two-dimensional magnet $CrCl_3$, Nat. Commun. **12**, 185 (2021).

[26] M. Ashton, D. Gluhovic, S. B. Sinnott, J. Guo, D. A. Stewart, and R. G. Hennig, Two-dimensional intrinsic half-metals with large spin gaps, Nano Lett. **17**, 5251 (2017).

[27] Y. Yang, W. Wang, P. Moitra, I. I. Kravchenko, D. P. Briggs, and J. Valentine, Dielectric meta-reflect array for broadband linear polarization conversion and optical vortex generation, Nano Lett. **14**, 1394 (2014).

[28] T. Song, X. Cai, M. W.-Y. Tu, X. Zhang, B. Huang, N. P. Wilson, K. L. Seyler, L. Zhu, T. Taniguchi, K. Watanabe, M. A. McGuire, D. H. Cobden, D. Xiao, W. Yao, and X. Xu, Giant tunneling magnetoresistance in spin-filter van der Waals heterostructures, Science **360**, 1214 (2018).

[29] T. Song, M. W.-Y. Tu, C. Carnahan, X. Cai, T. Taniguchi, K. Watanabe, M. A. McGuire, D. H. Cobden, D. Xiao, W. Yao, and X. Xu, Voltage control of a van der Waals spin-filter magnetic tunnel junction, Nano Lett. **19**, 915 (2019).

[30] S. Jiang, L. Li, Z. Wang, J. Shan, and K. F. Mak, Spin tunnel field-effect transistors based on two-dimensional van der Waals heterostructures, Nat. Electron. **2**, 159 (2019).

[31] S.-J. Gong, C. Gong, Y.-Y. Sun, W.-Y. Tong, C.-G. Duan, J.-H. Chu, and X. Zhang, Electrically induced 2D half-metallic antiferromagnets and spin field effect transistors, Proc. Natl. Acad. Sci. USA **115**, 8511 (2018).

[32] M. A. McGuire, H. Dixit, V. R. Cooper, and B. C. Sales, Coupling of crystal structure and magnetism in the layered, ferromagnetic insulator CrI_3, Chem. Mater. **27**, 612 (2015).

[33] I. Tsubokawa, On the magnetic properties of a $CrBr_3$ single crystal, J. Phys. Soc. Jpn. **15**, 1664 (1960).

[34] B. Huang, G. Clark, E. Navarro-Moratalla, D. R. Klein, R. Cheng, K. L. Seyler, D. Zhong, E. Schmidgall, M. A. McGuire, D. H. Cobden, W. Yao, D. Xiao, P. Jarillo-Herrero, and X. Xu, Layer-dependent ferromagnetism in a van der Waals crystal down to the monolayer limit, Nature (London) **546**, 270 (2017).

[35] L. D. Casto, A. J. Clune, M. O. Yokosuk, J. L. Musfeldt, T. J. Williams, H. L. Zhuang, M.-W. Lin, K. Xiao, R. G. Hennig, B. C. Sales, J.-Q. Yan, and D. Mandrus, Strong spin-lattice coupling in $CrSiTe_3$, APL Mater. **3**, 041515 (2015).

[36] V. Carteaux, D. Brunet, G. Ouvrard, and G. Andre, Crystallographic, magnetic and electronic structures of a new layered ferromagnetic compound $Cr_2Ge_2Te_6$, J. Phys. Condens. Matter **7**, 69 (1995).

[37] C. Gong, L. Li, Z. Li, H. Ji, A. Stern, Y. Xia, T. Cao, W. Bao, C. Wang, Y. Wang, Z. Q. Qiu, R. J. Cava, S. G. Louie, J. Xia, and X. Zhang, Discovery of intrinsic ferromagnetism in two-dimensional van der Waals crystals, Nature (London) **546**, 265 (2017).

[38] K. K. Kim, Two-dimensional air-stable $CrSe_2$ nanosheets with thickness-tunable magnetism, J. Semicond. **42**, 100401 (2021).

[39] B. Li, Z. Wan, C. Wang, P. Chen, B. Huang, X. Cheng, Q. Qian, J. Li, Z. Zhang, G. Sun, B. Zhao, H. Ma, R. Wu, Z. Wei, Y. Liu, L. Liao, Y. Ye, Y. Huang, X. Xu, X. Duan, W. Ji, and X. Duan, Van der Waals epitaxial growth of air-stable $CrSe_2$ nanosheets with thickness-tunable magnetic order, Nat. Mater. **20**, 818 (2021).

[40] D. Chiba, K. Takamura, F. Matsukura, and H. Ohno, Effect of low-temperature annealing on (Ga,Mn)As trilayer structures, Appl. Phys. Lett. **82**, 3020 (2003).

[41] I. Hwang, M. J. Coak, N. Lee, D.-S. Ko, Y. Oh, I. Jeon, S. Son, K. Zhang, J. Kim, and J.-G. Park, Hard ferromagnetic van-der-Waals metal $(Fe, Co)_3GeTe_2$: A new platform for the study of low-dimensional magnetic quantum criticality, J. Phys. Condens. Matter **31**, 50LT01 (2019).

[42] Y. Zhao, J. Gu, and Z. Chen, Oxygen evolution reaction on 2D ferromagnetic Fe_3GeTe_2: Boosting the reactivity by the self-reduction of surface hydroxyl, Adv. Funct. Mater. **29**, 1904782 (2019).

[43] L. Alahmed, B. Nepal, J. Macy, W. Zheng, B. Casas, A. Sapkota, N. Jones, A. R. Mazza, M. Brahlek, W. Jin, M. Mahjouri-Samani, S. S.-L. Zhang, C. Mewes, L. Balicas, T. Mewes, and P. Li, Magnetism and spin dynamics in room-temperature van der Waals magnet Fe_5GeTe_2, 2D Mater. **8**, 045030 (2021).

[44] J. Seo, D. Y. Kim, E. S. An, K. Kim, G.-Y. Kim, S.-Y. Hwang, D. W. Kim, B. G. Jang, H. Kim, G. Eom, S. Y. Seo, R. Stania, M. Muntwiler, J. Lee, K. Watanabe, T. Taniguchi, Y. J. Jo, J. Lee, B. I. Min, M. H. Jo, H. W. Yeom, S.-Y. Choi, J. H. Shim, and J. S. Kim, Nearly room temperature ferromagnetism in a magnetic metal-rich van der Waals metal, Sci. Adv. **6**, eaay8912 (2020).

[45] G. Zhang, F. Guo, H. Wu, X. Wen, L. Yang, W. Jin, W. Zhang, and H. Chang, Above-room-temperature strong intrinsic ferromagnetism in 2D van der Waals Fe_3GaTe_2 with large perpendicular magnetic anisotropy, Nat. Commun. **13**, 5067 (2022).

[46] D. C. Freitas, R. Weht, A. Sulpice, G. Remenyi, P. Strobel, F. Gay, J. Marcus, and M. Núñez-Regueiro, Ferromagnetism in layered metastable 1T-$CrTe_2$, J. Phys. Condens. Matter **27**, 176002 (2015).

[47] D. J. O'Hara, T. Zhu, A. H. Trout, A. S. Ahmed, Y. K. Luo, C. H. Lee, M. R. Brenner, S. Rajan, J. A. Gupta, D. W.

McComb, and R. K. Kawakami, Room temperature intrinsic ferromagnetism in epitaxial manganese selenide films in the monolayer limit, Nano Lett. **18**, 3125 (2018).

[48] Y. Wang, C. Wang, S. Liang, Z. Ma, K. Xu, X. Liu, L. Zhang, A. S. Admasu, S. Cheong, L. Wang, M. Chen, Z. Liu, B. Cheng, W. Ji, and F. Miao, Strain-sensitive magnetization reversal of a van der Waals magnet, Adv. Mater. **32**, 2004533 (2020).

[49] G. Cheng, M. M. Rahman, Z. He, A. L. Allcca, A. Rustagi, K. A. Stampe, Y. Zhu, S. Yan, S. Tian, Z. Mao, H. Lei, K. Watanabe, T. Taniguchi, P. Upadhyaya, and Y. P. Chen, Emergence of electric-field-tunable interfacial ferromagnetism in 2D antiferromagnet heterostructures, Nat. Commun. **13**, 7348 (2022).

[50] L. Zhang, X. Huang, H. Dai, M. Wang, H. Cheng, L. Tong, Z. Li, X. Han, X. Wang, L. Ye, and J. Han, Proximity-coupling-induced significant enhancement of coercive field and Curie temperature in 2D van der Waals heterostructures, Adv. Mater. **32**, 2002032 (2020).

[51] M. Bonilla, S. Kolekar, Y. Ma, H. C. Diaz, V. Kalappattil, R. Das, T. Eggers, H. R. Gutierrez, M.-H. Phan, and M. Batzill, Strong room-temperature ferromagnetism in VSe_2 monolayers on van der Waals substrates, Nat. Nanotechnol. **13**, 289 (2018).

[52] L. F. Kourkoutis, J. H. Song, H. Y. Hwang, and D. A. Muller, Microscopic origins for stabilizing room-temperature ferromagnetism in ultrathin manganite layers, Proc. Natl. Acad. Sci. USA **107**, 11682 (2010).

[53] J. Yang, X. Wang, S. Li, X. Wang, M. Pan, M. Ai, H. Yuan, X. Peng, R. Wang, Q. Li, F. Zheng, and P. Zhang, Robust two-dimensional ferromagnetism in $Cr_5Te_8/CrTe_2$ heterostructure with Curie temperature above 400 K, ACS Nano **17**, 23160 (2023).

[54] S. Jiang, L. Li, Z. Wang, K. F. Mak, and J. Shan, Controlling magnetism in 2D CrI_3 by electrostatic doping, Nat. Nanotechnol. **13**, 549 (2018).

[55] B. Huang, G. Clark, D. R. Klein, D. MacNeill, E. Navarro-Moratalla, K. L. Seyler, N. Wilson, M. A. McGuire, D. H. Cobden, D. Xiao, W. Yao, P. Jarillo-Herrero, and X. Xu, Electrical control of 2D magnetism in bilayer CrI_3, Nat. Nanotechnol. **13**, 544 (2018).

[56] W. Hu, C. Wang, H. Tan, H. Duan, G. Li, N. Li, Q. Ji, Y. Lu, Y. Wang, Z. Sun, F. Hu, and W. Yan, Embedding atomic cobalt into graphene lattices to activate room-temperature ferromagnetism, Nat. Commun. **12**, 1854 (2021).

[57] L. Yang, H. Wu, L. Zhang, W. Zhang, L. Li, T. Kawakami, K. Sugawara, T. Sato, G. Zhang, P. Gao, Y. Muhammad, X. Wen, B. Tao, F. Guo, and H. Chang, Highly tunable near-room temperature ferromagnetism in Cr-Doped layered Td-WTe_2, Adv. Funct. Mater. **31**, 2008116 (2021).

[58] X. Chen, Y.-T. Shao, R. Chen, S. Susarla, T. Hogan, Y. He, H. Zhang, S. Wang, J. Yao, P. Ercius, D. A. Muller, R. Ramesh, and R. J. Birgeneau, Pervasive beyond room-temperature ferromagnetism in a doped van der Waals magnet, Phys. Rev. Lett. **128**, 217203 (2022).

[59] F. C. Chen, Y. Fei, S. J. Li, Q. Wang, X. Luo, J. Yan, W. J. Lu, P. Tong, W. H. Song, X. B. Zhu, L. Zhang, H. B. Zhou, F. W. Zheng, P. Zhang, A. L. Lichtenstein, M. I. Katsnelson, Y. Yin, N. Hao, and Y. P. Sun, Temperature-induced Lifshitz transition and possible excitonic instability in ZrSiSe, Phys. Rev. Lett. **124**, 236601 (2020).

[60] H. Chi, C. Zhang, G. Gu, D. E. Kharzeev, X. Dai, and Q. Li, Lifshitz transition mediated electronic transport anomaly in bulk $ZrTe_5$, New J. Phys. **19**, 015005 (2017).

[61] Y. Shi, S. Che, K. Zhou, S. Ge, Z. Pi, T. Espiritu, T. Taniguchi, K. Watanabe, Y. Barlas, R. Lake, and C. N. Lau, Tunable Lifshitz transitions and multiband transport in tetralayer graphene, Phys. Rev. Lett. **120**, 096802 (2018).

[62] A. Varlet, D. Bischoff, P. Simonet, K. Watanabe, T. Taniguchi, T. Ihn, K. Ensslin, M. Mucha-Kruczyński, and V. I. Fal'ko, Anomalous sequence of quantum Hall liquids revealing a tunable Lifshitz transition in bilayer graphene, Phys. Rev. Lett. **113**, 116602 (2014).

[63] Y. Wu, N. H. Jo, M. Ochi, L. Huang, D. Mou, S. L. Bud'ko, P. C. Canfield, N. Trivedi, R. Arita, and A. Kaminski, Temperature-induced Lifshitz transition in WTe_2, Phys. Rev. Lett. **115**, 166602 (2015).

[64] Y. Wang, M. Zhao, J. Zhang, W. Wu, S. Li, Y. Zhang, W. Jiang, N. B. Joseph, L. Xu, Y. Mou, Y. Yang, P. Leng, Y. Zhang, L. Pi, A. Suslov, M. Ozerov, J. Wyzula, M. Orlita, F. Zhu, Y. Zhang, X. Kou, Z. Zhu, A. Narayan, D. Qian, J. Wen, X. Yuan, F. Xiu, and C. Zhang, Observation of quantum oscillations near the Mott-Ioffe-Regel limit in $CaAs_3$, Natl. Sci. Rev. **11**, nwae127 (2024).

[65] S. Manzeli, D. Ovchinnikov, D. Pasquier, O. V. Yazyev, and A. Kis, 2D transition metal dichalcogenides, Nat. Rev. Mater. **2**, 17033 (2017).

[66] X. Xu, W. Yao, D. Xiao, and T. F. Heinz, Spin and pseudospins in layered transition metal dichalcogenides, Nat. Phys. **10**, 343 (2014).

[67] W. Ruan, Y. Chen, S. Tang, J. Hwang, H.-Z. Tsai, R. L. Lee, M. Wu, H. Ryu, S. Kahn, F. Liou, C. Jia, A. Aikawa, C. Hwang, F. Wang, Y. Choi, S. G. Louie, P. A. Lee, Z.-X. Shen, S.-K. Mo, and M. F. Crommie, Evidence for quantum spin liquid behaviour in single-layer 1T-$TaSe_2$ from scanning tunnelling microscopy, Nat. Phys. **17**, 1154 (2021).

[68] H. N. S. Lee, M. Garcia, H. McKinzie, and A. Wold, The low-temperature electrical and magnetic properties of $TaSe_2$, and $NbSe_2$, J. Solid State Chem. **1**, 190 (1970).

[69] Y. Chen, W. Ruan, M. Wu, S. Tang, H. Ryu, H.-Z. Tsai, R. L. Lee, S. Kahn, F. Liou, C. Jia, O. R. Albertini, H. Xiong, T. Jia, Z. Liu, J. A. Sobota, A. Y. Liu, J. E. Moore, Z.-X. Shen, S. G. Louie, S.-K. Mo, and M. F. Crommie, Strong correlations and orbital texture in single-layer 1T-$TaSe_2$, Nat. Phys. **16**, 218 (2020).

[70] J. Feng, D. Biswas, A. Rajan, M. D. Watson, F. Mazzola, O. J. Clark, K. Underwood, I. Markovic, M. McLaren, A. Hunter, D. M. Burn, L. B. Duffy, S. Barua, G. Balakrishnan, F. Bertran, P. Le Fevre, T. K. Kim, G. van der Laan, T. Hesjedal, P. Wahl, and P. D. C. King, Electronic structure and enhanced charge-density wave order of monolayer VSe_2, Nano Lett. **18**, 4493 (2018).

[71] J. Yang, W. Wang, Y. Liu, H. Du, W. Ning, G. Zheng, C. Jin, Y. Han, N. Wang, Z. Yang, M. Tian, and Y. Zhang, Thickness dependence of the charge-density-wave transition temperature in VSe_2, Appl. Phys. Lett. **105**, 063109 (2014).

[72] P. M. Coelho, K. Nguyen Cong, M. Bonilla, S. Kolekar, M.-H. Phan, J. Avila, M. C. Asensio, I. I. Oleynik, and M. Batzill, Charge density wave state suppresses ferromagnetic ordering in VSe_2 monolayers, J. Phys. Chem. C **123**, 14089 (2019).

[73] A. O. Fumega, M. Gobbi, P. Dreher, W. Wan, C. González-Orellana, M. Peña-Díaz, C. Rogero, J. Herrero-Martín, P. Gargiani, M. Ilyn, M. M. Ugeda, V. Pardo, and S. Blanco-Canosa, Absence of ferromagnetism in VSe_2 caused by its charge density wave phase, J. Phys. Chem. C **123**, 27802 (2019).

[74] J.-A. Yan, M. A. D. Cruz, B. Cook, and K. Varga, Structural, electronic and vibrational properties of few-layer 2H- and 1T-$TaSe_2$, Sci. Rep. **5**, 16646 (2015).

[75] J. Pandey and A. Soni, Electron-phonon interactions and two-phonon modes associated with charge density wave in single crystalline 1T-VSe_2, Phys. Rev. Res. **2**, 033118 (2020).

[76] X. Meng, Y. Du, W. Wu, N. B. Joseph, X. Deng, J. Wang, J. Ma, Z. Shi, B. Liu, Y. Ma, F. Yue, N. Zhong, P. Xiang, C. Zhang, C. Duan, A. Narayan, Z. Sun, J. Chu, and X. Yuan, Giant superlinear power dependence of photocurrent based on layered Ta_2NiS_5 photodetector, Adv. Sci. **10**, 2300413 (2023).

[77] Y. Du, J. Chen, W. Wu, Z. Shi, X. Meng, C. Zhang, S. Gong, J. Chu, and X. Yuan, Comparative Raman spectroscopy of magnetic topological material $EuCd_2X_2$ (X = P, As), J. Phys.: Condens. Matter **34**, 224001 (2022).

[78] S. Sugai, K. Murase, S. Uchida, and S. Tanaka, Investigation of the charge density waves in 1T-VSe_2 by Raman scattering, Le Journal De Physique Colloques **42**, C6-740 (1981).

[79] H.-S. Tsai, F.-W. Liu, J.-W. Liou, C.-C. Chi, S.-Y. Tang, C. Wang, H. Ouyang, Y.-L. Chueh, C. Liu, S. Zhou, and W.-Y. Woon, Direct synthesis of large-scale multilayer $TaSe_2$ on SiO_2/Si using ion beam technology, ACS Omega **4**, 17536 (2019).

[80] H. Luo, W. Xie, J. Tao, I. Pletikosic, T. Valla, G. Osterhoudt, E. Sutton, K. S. Burch, J. W. Krizan, Y. Zhu, and R. J. Cava, Differences in chemical doping matter - Superconductivity in $Ti_{1-x}Ta_xSe_2$ but not in $Ti_{1-x}Nb_xSe_2$, Chem. Mater. **28**, 1927 (2016).

[81] C. J. Sayers, L. S. Farrar, S. J. Bending, M. Cattelan, A. J. H. Jones, N. A. Fox, G. Kociok-Köhn, K. Koshmak, J. Laverock, L. Pasquali, and E. Da Como, Correlation between crystal purity and the charge density wave in 1T-VSe_2, Phys. Rev. Mater. **4**, 025002 (2020).

[82] F. Tang, Y. Ren, P. Wang, R. Zhong, J. Schneeloch, S. A. Yang, K. Yang, P. A. Lee, G. Gu, Z. Qiao, and L. Zhang, Three-dimensional quantum Hall effect and metal–insulator transition in $ZrTe_5$, Nature (London) **569**, 537 (2019).

[83] P. Knowles, B. Yang, T. Muramatsu, O. Moulding, J. Buhot, C. J. Sayers, E. Da Como, and S. Friedemann, Fermi surface reconstruction and electron dynamics at the charge-density-wave transition in $TiSe_2$, Phys. Rev. Lett. **124**, 167602 (2020).

[84] Y. Deng, Y. Yu, Y. Song, J. Zhang, N. Z. Wang, Z. Sun, Y. Yi, Y. Z. Wu, S. Wu, J. Zhu, J. Wang, X. H. Chen, and Y. Zhang, Gate-tunable room-temperature ferromagnetism in two-dimensional Fe_3GeTe_2, Nature (London) **563**, 94 (2018).

[85] S. Friedli and Y. Velenik, *Statistical Mechanics of Lattice Systems: A Concrete Mathematical Introduction* (Cambridge University Press, Cambridge, England, 2017).

[86] Y. Cao and C. Zhou, Dependence of coercivity on ferromagnetic layer thickness in FeNiCr/Cr bilayers, J. Magn. Magn. Mater. **369**, 5 (2014).

[87] G. Suran, H. Ouahmane, and J. Sztern, Coercive field of amorphous soft ferromagnetic films: Dependence upon thickness, J. Magn. Magn. Mater. **140-144**, 691 (1995).

[88] S. Kumari, D. K. Pradhan, N. R. Pradhan, and P. D. Rack, Recent developments on 2D magnetic materials: Challenges and opportunities, Emergent Mater. **4**, 827 (2021).

[89] K. T. Li and V. C. Lo, Simulation of thickness dependence in ferroelectric thin films, Solid State Commun. **132**, 49 (2004).

[90] P. Chandra, M. Dawber, P. B. Littlewood, and J. F. Scott, Thickness-dependence of the coercive field in ferroelectrics, arXiv:cond-mat/0206014.

[91] Z. Fei, B. Huang, P. Malinowski, W. Wang, T. Song, J. Sanchez, W. Yao, D. Xiao, X. Zhu, A. F. May, W. Wu, D. H. Cobden, J.-H. Chu, and X. Xu, Two-dimensional itinerant ferromagnetism in atomically thin Fe_3GeTe_2, Nat. Mater. **17**, 778 (2018).

[92] R. Fujita, P. Bassirian, Z. Li, Y. Guo, M. A. Mawass, F. Kronast, G. van der Laan, and T. Hesjedal, Layer-dependent magnetic domains in atomically thin Fe_5GeTe_2, ACS Nano **16**, 10545 (2022).

[93] Q. Li, M. Yang, C. Gong, R. V. Chopdekar, A. T. N'Diaye, J. Turner, G. Chen, A. Scholl, P. Shafer, E. Arenholz, A. K. Schmid, S. Wang, K. Liu, N. Gao, A. S. Admasu, S.-W. Cheong, C. Hwang, J. Li, F. Wang, X. Zhang, and Z. Qiu, Patterning-induced ferromagnetism of Fe_3GeTe_2 van der Waals materials beyond room temperature, Nano Lett. **18**, 5974 (2018).

[94] A. Jain, S. P. Ong, G. Hautier, W. Chen, W. D. Richards, S. Dacek, S. Cholia, D. Gunter, D. Skinner, G. Ceder, and K. A. Persson, Commentary: The Materials Project: A materials genome approach to accelerating materials innovation, APL Mater. **1**, 011002 (2013).

[95] H.-R. Fuh, B. Yan, S.-C. Wu, C. Felser, and C.-R. Chang, Metal-insulator transition and the anomalous Hall effect in the layered magnetic materials VS_2 and VSe_2, New J. Phys. **18**, 113038 (2016).

[96] J. Gao, Y. Cheng, T. Tian, X. Hu, K. Zeng, G. Zhang, and Y.-W. Zhang, Structure, stability, and kinetics of vacancy defects in monolayer $PtSe_2$: A first-principles study, ACS Omega **2**, 8640 (2017).

[97] J. Li, T. Joseph, M. Ghorbani-Asl, S. Kolekar, A. V. Krasheninnikov, and M. Batzill, Edge and point-defect induced electronic and magnetic properties in monolayer $PtSe_2$, Adv. Funct. Mater. **32**, 2110428 (2022).

[98] P. Manchanda, P. Kumar, and P. Dev, Defect-induced 4p-magnetism in layered platinum diselenide, Phys. Rev. B **103**, 144403 (2021).

[99] A. Avsar, A. Ciarrocchi, M. Pizzochero, D. Unuchek, O. V. Yazyev, and A. Kis, Defect induced, layer-modulated magnetism in ultrathin metallic $PtSe_2$, Nat. Nanotechnol. **14**, 674 (2019).

[100] R. Chua, J. Yang, X. He, X. Yu, W. Yu, F. Bussolotti, P. K. J. Wong, K. P. Loh, M. B. H. Breese, K. E. J. Goh, Y. L. Huang, and A. T. S. Wee, Can reconstructed Se-deficient line defects in monolayer VSe_2 induce magnetism? Adv. Mater. **32**, 2000693 (2020).

[101] P. Manchanda and R. Skomski, Defect-induced magnetism in two-dimensional $NbSe_2$, Superlattices Microstruct. **101**, 349 (2017).

[102] K. Momma and F. Izumi, VESTA: A three-dimensional visualization system for electronic and structural analysis, J. Appl. Crystallogr. **41**, 653 (2008).

[103] G. Kresse and J. Furthmüller, Efficiency of ab-initio total energy calculations for metals and semiconductors using a plane-wave basis set, Comput. Mater. Sci. **6**, 15 (1996).

[104] J. Hafner, *Ab-initio* simulations of materials using VASP: Density-functional theory and beyond, J. Comput. Chem. **29**, 2044 (2008).

[105] J. P. Perdew, K. Burke, and M. Ernzerhof, Generalized gradient approximation made simple, Phys. Rev. Lett. **77**, 3865 (1996).

[106] V. I. Anisimov, I. V. Solovyev, M. A. Korotin, M. T. Czyżyk, and G. A. Sawatzky, Density-functional theory and NiO photoemission spectra, Phys. Rev. B **48**, 16929 (1993).